AGU PUBLICATIONS

Geophysical Research Letters

RESEARCH LETTER
10.1002/2015GL063287

Key Points:
- Accurate, timely irradiance estimates are vital for remote ocean spectroscopy
- Reference targets constrain the apparent irradiance from 380 to 600 nm
- Improved retrieval accuracy is demonstrated across multiple airborne instruments

Supporting Information:
- Text S1
- Data Set S1

Correspondence to:
D. R. Thompson,
david.r.thompson@jpl.nasa.gov

Citation:
Thompson, D. R., F. C. Seidel, B. C. Gao, M. M. Gierach, R. O. Green, R. M. Kudela, and P. Mouroulis (2015), Optimizing irradiance estimates for coastal and inland water imaging spectroscopy, *Geophys. Res. Lett.*, *42*, 4116–4123, doi:10.1002/2015GL063287.

Received 1 FEB 2015
Accepted 5 MAY 2015
Accepted article online 9 MAY 2015
Published online 29 MAY 2015

©2015. American Geophysical Union. All Rights Reserved.

Optimizing irradiance estimates for coastal and inland water imaging spectroscopy

David R. Thompson[1], Felix C. Seidel[1], Bo Cai Gao[2], Michelle M. Gierach[1], Robert O. Green[1], Raphael M. Kudela[3], and Pantazis Mouroulis[1]

[1] Jet Propulsion Laboratory, California Institute of Technology, Pasadena, California, USA, [2] U.S. Naval Research Laboratory, Washington, District of Columbia, USA, [3] University of California Santa Cruz, Santa Cruz, California, USA

Abstract Next generation orbital imaging spectrometers, with advanced global remote sensing capabilities, propose to address outstanding ocean science questions related to coastal and inland water environments. These missions require highly accurate characterization of solar irradiance in the critical 380–600 nm spectral range. However, the irradiance in this spectral region is temporally variable and difficult to measure directly, leading to considerable variance between different models. Here we optimize an irradiance estimate using data from the NASA airborne Portable Remote Imaging Spectrometer (PRISM), leveraging spectrally smooth in-scene targets. We demonstrate improved retrievals for both PRISM and the Next Generation Airborne Visible Infrared Imaging Spectrometer.

1. Introduction

Airborne imaging spectrometers play a unique role for mapping coastal and inland systems, while serving as precursors for future orbital missions such as the Hyperspectral Infrared Imager and Pre-Aerosol, Cloud, and ocean Ecosystem spacecraft. The spectral imaging data to be acquired from these missions will be used to derive water-leaving radiance and the related quantity, remote sensing reflectance, R_{rs}, at high spectral resolution over wide areas. These signals carry information about the chemistry and size of suspended particles, as well as the composition and health of phytoplankton populations [*Lee et al.*, 2001; *Davis et al.*, 2002]. A growing family of spectrometers is designed specifically for coastal and inland water applications, including the NASA airborne Portable Remote Imaging Spectrometer (PRISM) [*Mouroulis et al.*, 2014] that offers higher signal-to-noise ratio (SNR) and improved spectral resolution in the critical 380–600 nm range. Coastal applications raise special challenges, including low SNR due to strong absorption by coastal waters and the complex optical constituents; poor knowledge of path radiance due to atmospheric aerosols, complicated by the failure of traditional dark pixel constraints in the presence of sunglint, turbidity, or benthic reflections [*Hochberg et al.*, 2011]; and calibration that relies on red-rich illumination standards [*Kohler et al.*, 2004].

These well-studied confounders typically manifest as spectrally smooth perturbations, while fine-scale perturbations have received less attention. This is surprising, since a major advantage of spectroscopy lies in the use of relative spectral peaks and shapes to characterize phytoplankton functional and taxonomic groups. Pigmentation absorption and backscatter signatures can potentially differentiate functional groups, significantly improving our understanding of ecosystem state and dynamics [*Aiken et al.*, 2008]. Recent studies use libraries of high-resolution R_{rs} features to classify phytoplankton involved in harmful algal blooms. These methods hold promise for wide-area mapping by orbital data [*Warner and Fan*, 2013]. For such applications, fine-scale perturbations are equally significant to the more commonly studied smooth effects. One likely source of fine-scale errors is uncertainty in solar irradiance, which is both spectrally and temporally variable from 380 to 600 nm. These solar lines can deepen or attenuate at different rates during the 11 year and 27 day activity cycles [*Marchenko and DeLand*, 2014]. Irradiance is challenging to measure directly, and discrepancies among contemporary models reach 1–5% [*Chance and Kurucz*, 2010] which is of comparable magnitude to the water-leaving radiance signal. Furthermore, the fine-scale spectral discontinuities are extremely sensitive to spectral calibration uncertainties or cross-track changes in instrument spectral response.

This work demonstrates that uncertainties in solar irradiance can be a significant source of fine-scale errors in coastal R_{rs} retrievals. We focus on PRISM data in the UV and visible ranges, which contain the dominant absorbing components for assessing phytoplankton pigmentation, biomass, and functional/taxonomic groups. We examine performance by an ensemble of four standard solar irradiance models: (1) the ATmospheric REMoval

(ATREM) adopted solar spectrum used in *Thompson et al.* [2015], which employs the MODTRAN 5.2 spectra of *Kurucz* [2005] at visible wavelengths; (2) the solar spectrum of *Thuillier et al.* [2003] based on direct extraterrestrial measurements by the ATLAS and SOLSPEC instruments; (3) the Visible-UV spectrum of *Chance and Kurucz* [2010]; and (4) the model-derived solar spectrum of *Fontenla et al.* [2011], which accounts for variability in the solar cycle.

A smooth in-scene reference is used to form an optimized instrument- and time-specific irradiance spectrum. The optimized solution significantly improves R_{rs} retrievals for multiple airborne instruments, targets and imaging conditions, and also generalizes across instruments with different spectral sampling. This provides a new solar spectrum for airborne spectroscopy, and more generally, a method to recover R_{rs} signatures smaller than the differences in available irradiance models.

2. Method

2.1. Optimization Procedure

The proposed approach uses a bright smooth target measured in close temporal proximity to the science data. Here we used a uniform concrete patch at the Grand Junction, WY airport. First the surface was measured with a Visible Shortwave Infrared (VSWIR) field spectrometer from PANalytical B. V., known formerly as Analytical Spectral Devices (ASD). The spectrometer produced 16 bit radiance data at 3 nm spectral resolution in the visible range. We calculated surface reflectance using a white spectralon panel to verify spectral smoothness. PRISM then overflew the same target on 16 April 2014 at an altitude of 1960 m (just 110 m above ground level). It acquired 14 bit data at 3 nm spectral resolution across the entire 380–1050 nm range, but we optimized only the 380–600 nm interval to minimize interference from atmospheric absorption features. After acquisition we processed the raw data using a standard PRISM radiometric calibration derived from laboratory measurements. The radiometric calibration was set by a white spectralon panel illuminated under known geometry by a National Institute of Standards and Technology standard lamp. The wavelength and full width at half maximum (FWHM) of each channel were also characterized in the laboratory using a process detailed in *Mouroulis et al.* [2014]. The wavelength calibration was further refined from flight data by least squares fitting of a gas transmission model to the oxygen A band feature at 760 nm. This process was sensitive to perturbations of less than 5% of the FWHM. We further verified accuracy of the wavelength calibration by manually tuning across a range of small offsets to ensure it had minimized residuals due to solar and atmospheric gas absorption lines.

After radiometric calculations, an initial reflectance result was derived using the *Chance and Kurucz* [2010] spectrum. We estimated R_{rs} by correcting measured radiances for atmospheric scattering and absorption. Following previous work [*Gao and Davis*, 1997; *Thompson et al.*, 2015], we calculated a top of atmosphere reflectance ρ for each channel (wavelength dependence omitted for clarity):

$$\rho = \frac{\pi L}{F_o \cos(\theta)} = T_g \left[r_a + \frac{\pi R_{rs} T_d T_u}{(1 - s\pi R_{rs})} \right] \tag{1}$$

L was the measured radiance, and θ the solar zenith angle. T_u, and T_d, respectively, represented the upward and downward transmission due to aerosol and molecular scattering. T_g was the total gaseous absorption based on a model 20-layer atmosphere with relevant absorbing gases such as NO_2, O_3, O_2, and H_2O. The variable s was the isotropic spherical albedo of the sky, and r_a was the reflectance of the atmosphere, commonly treated as a path radiance. We modeled all scattering terms using the 6s code as in *Gao and Davis* [1997]. F_o represented the extraterrestrial solar irradiance, which was stored at 1 cm^{-1}. Resampling solar spectra to instrument wavelengths without introducing artifacts required special care. We adopted a two-stage process used historically by the ATREM codebase as well as in *Gao and Davis* [1997]. Irradiances were first smoothed to a high resolution 0.2 nm grid using a Gaussian averaging kernel, and then downsampled to instrument wavelengths by convolving the spectral response function. Equation (1) gave the following Lambertian approximation for R_{rs}:

$$R_{rs} = \frac{\rho/T_g - r_a}{T_d T_u + s(\rho/T_g - r_a)} \frac{1}{\pi} \tag{2}$$

As expected, nearly all terms were spectrally smooth to within 0.5% or less in the 380–600 nm spectral range (Figure 1). Other factors not shown in Figure 1, such as the radiometric channel calibration coefficients and

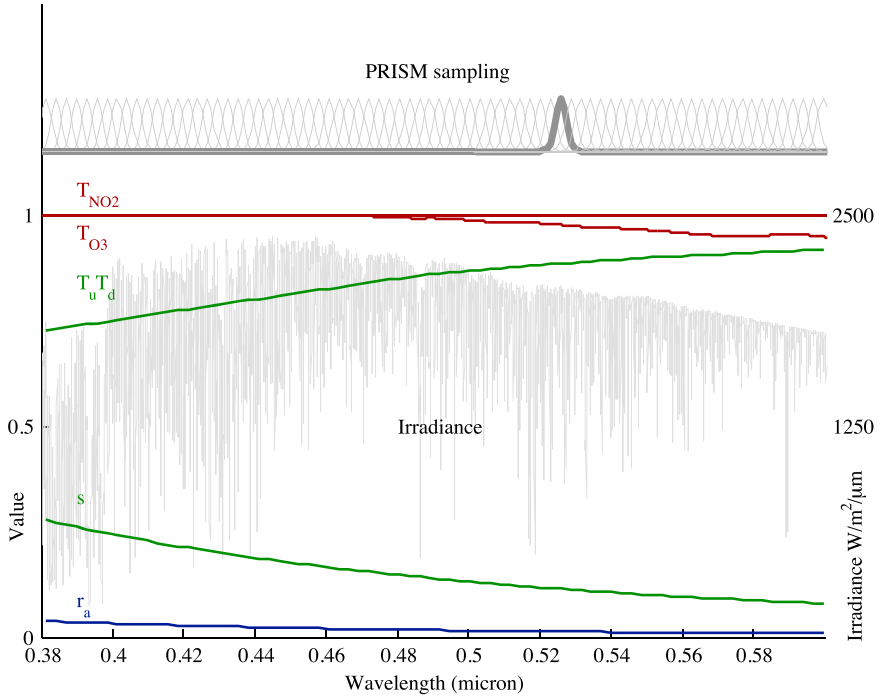

Figure 1. Solar irradiance is the most probable cause of fine spectral perturbations in the 0.3–0.6 μm region. Lines on the plot reference different parts of equation (2). All are smooth except for the solar irradiance contribution.

R_{rs} of typical targets, also differed smoothly. Even unmodeled effects, such as coupling between absorption and scattering or non-Lambertian reflectance, involved these smooth terms. The intrinsic solar spectrum, incorporating uncertainty in the time-varying irradiance F_o and in the downsampling process, remains as the main candidate to explain fine-scale spectral systematic errors of magnitudes at or above 0.5–14% in this spectral range.

We quantified these systematic errors using the deviation between the retrieved R_{rs} and a spectrally smooth reference. Specifically, we minimized $\|f_\alpha(\mathbf{R}_{rs}) - \mathbf{R}_{rs}\|_2$, the root sum squared error (RSSE) against a target smoothed by a cubic smoothing spline $f\alpha$ (boldface notation indicates vector-valued variables). The RSSE was insensitive to the spline smoothing penalty α, which could be set manually to an appropriate order of magnitude. We adjusted the extraterrestrial solar irradiance by optimizing a vector of channelwise multiplicative correction factors $\mathbf{x}$. The adjustment was $\hat{\mathbf{F}}_o = \mathbf{x} * \mathbf{F}_o$ where $*$ was element-wise multiplication, and $\hat{\mathbf{F}}_o$ was the perturbed solar irradiance used to produce an improved reflectance spectrum, $\hat{\mathbf{R}}_{rs}$. This led to the objective function:

$$E(x) = \|f_\alpha(\mathbf{R}_{rs}) - \hat{\mathbf{R}}_{rs}(x)\|_2 + \beta\|\mathbf{x} - 1\|_2 \quad (3)$$

β was a small regularization coefficient to keep elements of $\mathbf{x}$ near unity. We defined one correction coefficient for each instrument channel and estimated local error derivatives numerically. This enabled a conjugate gradient optimization producing a corrected solar irradiance. Finally, we upsampled $\mathbf{x}$ to the original solar spectrum resolution, linearly interpolating the scaling from the $\mathbf{x}$ coefficients. We adjusted the coefficients using the Nelder-Mead Simplex algorithm so that the two-stage downsampling process would result in the intended $\hat{\mathbf{F}}_o$.

2.2. Experimental Evaluation

We evaluated the new irradiance for different R_{rs} retrievals from PRISM flights over Monterey Bay, CA. These flights took place on 23 April 2014 at an altitude of 5800 m, a very different aerosol and molecular scattering regime from the training case. Our scattering model used the default 6s continental aerosol model, with an aerosol optical depth (AOD) of 0.15 set by coincident in situ measurements from a Reagan sunphotometer. As a final step in the retrieval, we compensated for oceanic sunglint by estimating the spectrally uniform glint contribution from the dark 1000 nm channel [*Hochberg et al.*, 2011]. We compared retrieved R_{rs} of bright and

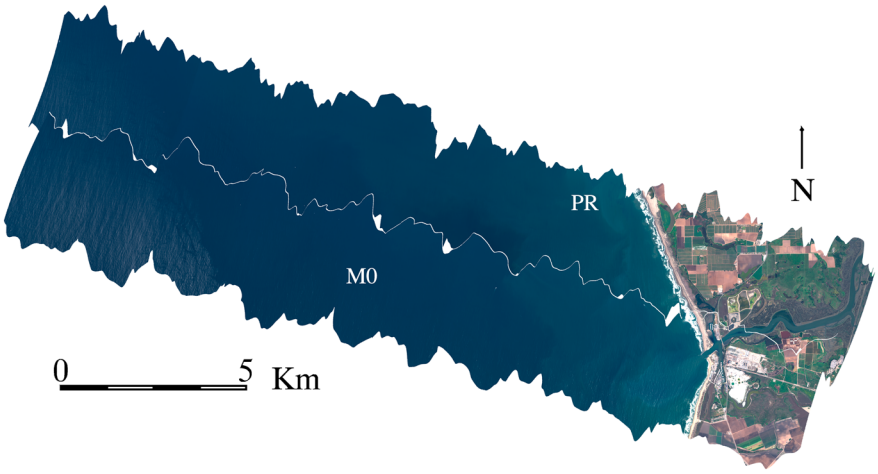

Figure 2. Monterey Bay validation flight lines showing M0 and Pajaro River mouth (PR) station locations at 36.8298°N, 121.8984°W and 36.8447°N, and 121.8262°W, respectively.

dark water targets to measurements by a HyperPro radiometer operated by a field team from the University of California (Santa Cruz). Spectra were measured at two reference stations in Monterey Bay: M0 and the Pajaro River mouth (Figure 2). The 16 bit HyperPro II data were collected using a minimum of three sequential profiles at each station, collected within approximately 15 min for all profiles at a station. Each cast was processed separately using Satlantic ProSoft (7.7.16_6) software. Data were binned to 0.1 m intervals, filtered to remove data with tilt >5°. Dark shutter corrections were applied, and a deck pressure-tare was employed. Processing parameters used *Thuillier et al.* [2003] extraterrestrial irradiance, reflection albedo of 0.043, reflectance and refractive indices of 0.021 and 1.345, and a minimum of five points for extrapolation to the surface. Remote sensing reflectance was calculated for each cast using the downwelling irradiance sensor and the surface reference sensor. Both stations had median coefficients of variation (across all wavelengths) of 10% with variance increasing (CV > 20% for some channels) for wavelengths greater than 700 nm. We extracted coincident spectra from georectified PRISM R_{rs} data, selecting an area approximately 150 m wide centered on each target location. We then performed an R_{rs} retrieval using each of the canonical irradiance reference sources, and quantified performance using the RSSE with respect to the smoothed reflectance. The *Fontenla et al.* [2011] model could account for different solar activity levels. We used a spectrum appropriate for high activity but found that the differences were small relative to discrepancies between sources.

In principle the irradiance optimization might incorporate sampling errors from the instrument-specific spectral response or stray light, in which case the irradiance optimization might not generalize to other instruments. To test this possibility, we applied the new irradiance to data from the Next Generation Airborne Visible Near Infrared Spectrometer (AVIRIS-NG). AVIRIS-NG [*Hamlin et al.*, 2010] is a full-range VSWIR spectrometer measuring 14 bit radiance from 380 to 2500 nm at 5 nm sampling. AVIRIS-NG flights took place in June 2014 over the Jet Propulsion Laboratory, an urban scene with multiple smooth reference targets. We collected in situ spectra of each target using a PANalytical spectrometer, with a leveled white spectralon panel as a well-characterized reference standard for reflectance calculations. After the flight, we calculated reflectances using each of the alternative irradiances. We not only used the standard AVIRIS-NG reflectance algorithm, which was similar to the PRISM approach, but also included dynamic estimation of pressure altitude and water vapor following *Thompson et al.* [2015]. There was no in situ measurement to constrain AOD, so a default clear-sky scenario with only molecular scattering was assumed.

3. Results

Figure 3 shows the reference irradiances, resampled to PRISM wavelengths using the two-stage approach. We have annotated features such as the CH + FeI blend at 429 nm and the CaII lines near 395 nm [*Wallace et al.*, 2011]. The converged solution stayed near the center of the ensemble, with no obvious systematic or asymmetric pattern to the direction of change for individual peaks or absorption lines. This was consistent with a physically meaningful (as opposed to instrument-related) correction.

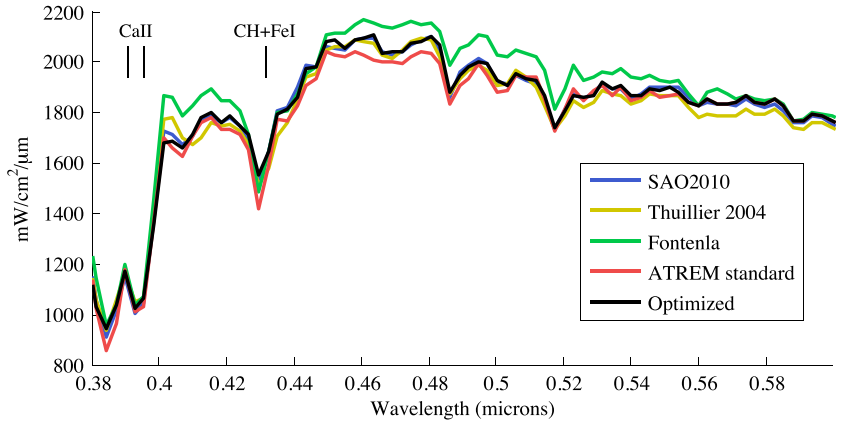

Figure 3. Prior and adjusted solar irradiance spectra (smoothed for clarity).

The new irradiance improved the accuracy of R_{rs} estimates for the validation targets. Figure 4 compares in situ and remote sensing retrieved R_{rs} at the Pajaro River mouth location. The optimized irradiance improved agreement at wavelengths shorter than 550 nm. Figure 4 (bottom) shows the residual difference between remote and in situ measurements, demonstrating a final agreement within 0.001 R_{rs} units over the 400–700 nm interval. Similar performance was observed for the M0 location in Figure 5, where the optimization improved residual spikes from 400 to 550 nm. In both cases the retrieval diverged sharply at the shortest wavelengths, an effect which could have been related to calibration uncertainties and is a topic of ongoing study. The in situ measurements are also less certain below 410 nm, where the HyperPro can be affected by stray sky irradiance that causes an unwanted upward "smile" in the reflectance spectrum. Next, Figure 6 shows the R_{rs} spectrum of an urban AVIRIS-NG asphalt target. We observe a uniform difference in brightness that could be related to aerosol effects or bidirectional reflectance of the asphalt or spectralon reference. However, standard irradiance models also produce fine-scale errors such as a relative dip at 400 nm near the CaII lines, and a peak at 430 nm near the FeI + CH blend. These features are similar to those in the high-resolution PRISM spectra and are similarly improved by the optimized irradiance.

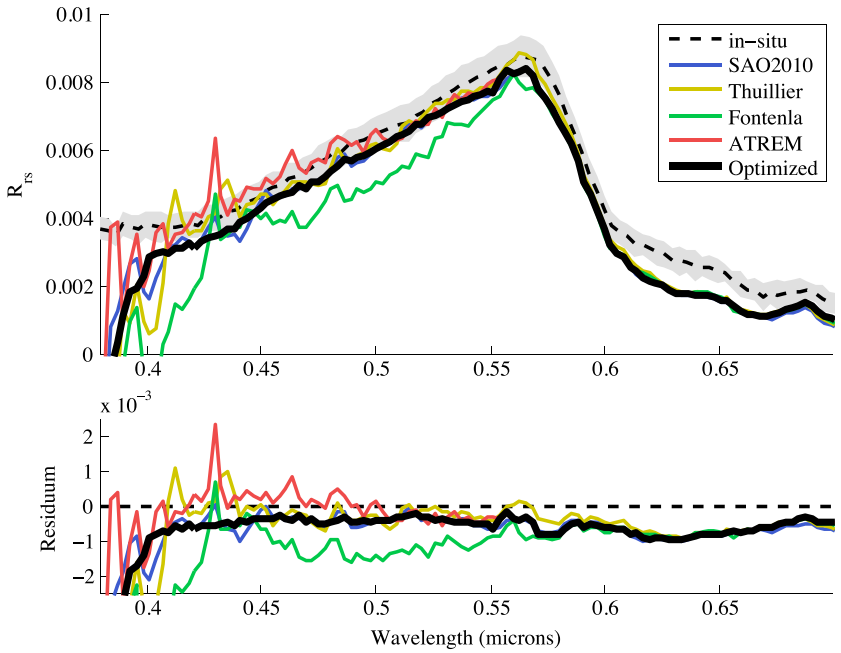

Figure 4. R_{rs} of water at the Pajaro River mouth location, comparing retrievals using prior solar irradiances as well as the optimized estimate. The grey band shows the standard deviation of acquisitions comprising the in situ spectrum. (top) Remote sensing reflectance. (bottom) Difference vs. the in situ measurement.

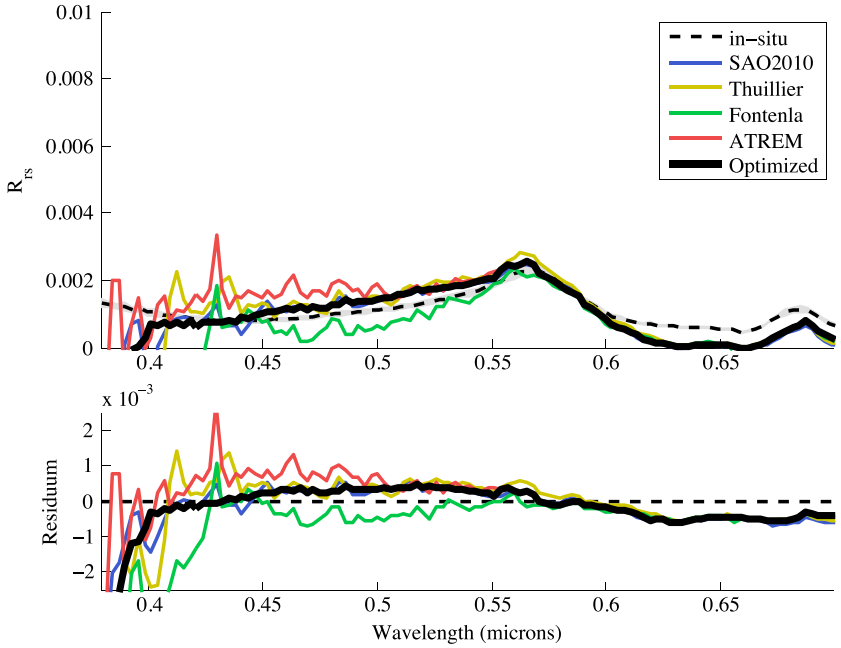

Figure 5. R_{rs} of water at the M0 location, comparing retrievals using prior solar irradiances as well as the optimized estimate. The grey band shows the standard deviation of acquisitions comprising the in situ spectrum.

Table 1 shows smoothness scores for all PRISM and AVIRIS-NG validation targets. The PRISM target at Grand Junction is a Dark Parking Lot (GJ DL). PRISM targets at Monterey Bay consist of Bright Water (MB BW), Dark Water (MB DW), Vegetation (V), and Sand (S), and validation targets at Pajaro River (MB PR) and M0 (MB M0), whose spectra are plotted in Figures 4 and 5. AVIRIS-NG targets include a Bright Parking Lot (JPL BL, 34.198289°N 118.172252°W) plotted in Figure 6, a bright Roof (JPL R, 34.198805°N, 118.171386°W), Dirt (JPL D, 34.202408°N 118.169884°W), and a Dark Parking Lot (JPL DL, 34.198594°N 118.172546°W). The optimized irradiance appears in boldface font and produces the smoothest retrievals in all cases. We note that flights

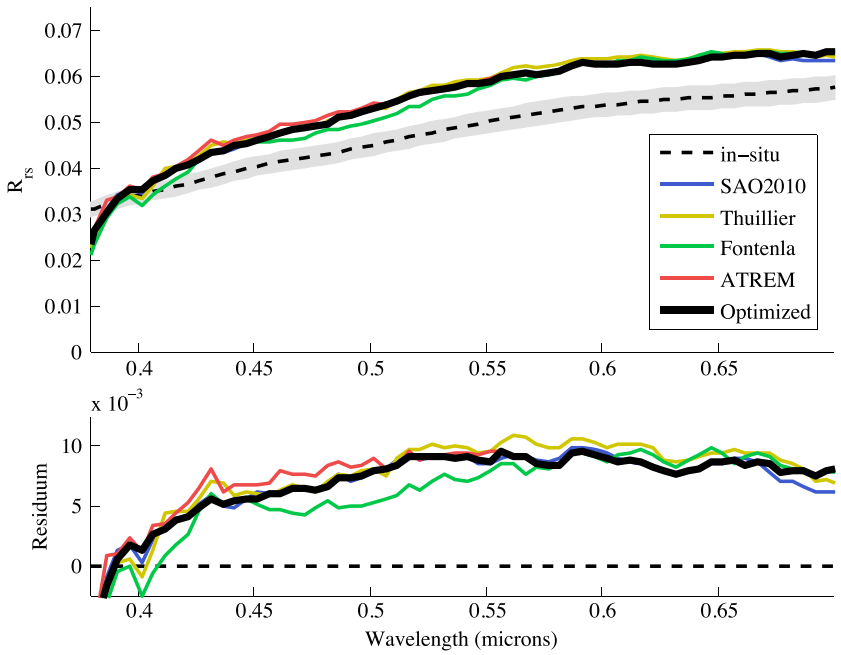

Figure 6. R_{rs} of a dark parking lot at the Jet Propulsion Laboratory, as estimated from AVIRIS-NG data. The grey band shows the standard deviation of reflectance measurements comprising the in situ spectrum.

Table 1. Performance of Different Solar Models Showing RSSE Relative to a Smoothed Standard[a]

Target	SAO	Thuillier	Fontenla	ATREM	Opt.
PRISM Spectra					
GJ DL	0.0037	0.0048	0.0055	0.0061	**0.0015**
MB BW	0.0091	0.0121	0.0147	0.0163	**0.0030**
MB DW	0.0073	0.0097	0.0122	0.0137	**0.0022**
MB V	0.0101	0.0128	0.0150	0.0168	**0.0055**
MB S	0.0177	0.0232	0.0264	0.0287	**0.0095**
MB PR	0.0086	0.0113	0.0140	0.0154	**0.0030**
MB M0	0.0078	0.0103	0.0131	0.0143	**0.0023**
AVIRIS-NG Spectra					
JPL BL	0.0160	0.0175	0.0173	0.0182	**0.0134**
JPL R	0.0219	0.0276	0.0228	0.0242	**0.0181**
JPL D	0.0145	0.0157	0.0156	0.0162	**0.0122**
JPL DL	0.0112	0.0121	0.0119	0.0129	**0.0095**

[a]Bold numerals indicate the smoothest spectrum in each trial.

span a wide range of altitudes: 100 m above Grand Junction, 5700 m above Monterey Bay, and 1700 m above the Jet Propulsion Laboratory. As a result, this collection represents a wide range of surfaces as well as atmospheric and scattering conditions.

4. Discussion

We conclude that (1) uncertainty in solar irradiance is a likely contributor to fine-scale spectral errors in R_{rs} retrievals; (2) there is considerable variability in existing models, manifesting as significant differences in spectral signatures for these wavelengths; and (3) an empirical optimization of solar irradiance can improve fine-scale discontinuities to enable more accurate recovery of spectral signatures. There is no algorithmic guarantee that the algorithm corrects only solar irradiance, and it may also compensate for errors in instrument spectral response or atmospheric correction. However, we find that the optimization improves retrievals for different instruments flying under different atmospheric scattering conditions. Advanced ocean remote sensing applications (such as discrimination of phytoplankton taxa) demand improved spectral resolution and sensitivity to UV wavelengths. This creates persistent need for reliable solar irradiance estimates. The demonstrated approach is a pragmatic path to address the inevitable uncertainties in instrument calibration and solar irradiance. Many land sites such as forests are also very dark in the 380–600 nm spectral range and could also benefit from this method. The methodology is generic and applies retroactively to instruments such as HICO [*Lucke et al.*, 2011] if in situ standards are available. It could also apply to future instruments such as ENMAP [*Stuffler et al.*, 2007]. The optimization would be most beneficial for instruments with high spectral resolution operating in UV wavelengths, where it can resolve the entangled uncertainties in fine-scale irradiance features and instrument spectral response.

Acknowledgments
The optimized irradiance spectrum and all PRISM and AVIRIS-NG radiance spectra are available at http://prism.jpl.nasa.gov and http://aviris-ng.jpl.nasa.gov. Data for Figures 3–6 are provided as supporting information. This research was performed at the Jet Propulsion Laboratory, California Institute of Technology, under a contract with the National Aeronautics and Space Administration. We thank the JPL PRISM team: D. Cohen, K. Balasubramanian, S. Leland, F. Loya, D. Moore, D. Randall, J. Rodriguez, C. Sarture, E. Urquiza, V. White, and K. Yee. We thank D. A. Roberts, E. Pennington, and B. Bue for assistance with AVIRIS-NG ground truth data. K. Hayashi Negrey of the University of California, Santa Cruz provided invaluable support with the collection of in situ reflectance data. We thank J. M. Fontenla for his counsel and assistance. We also thank B. Mateer, I. McCubbin, and C. V. White, and acknowledge the financial support of the JPL Earth System Science Formulation office.
Copyright 2015 California Institute of Technology. All Rights Reserved.

The Editor thanks Curtiss Davis and Robert Warner for their assistance in evaluating this paper.

References

Aiken, J., N. J. Hardman-Mountford, R. Barlow, J. Fishwick, T. Hirata, and T. Smyth (2008), Functional links between bioenergetics and bio-optical traits of phytoplankton taxonomic groups, *J. Plankton Res.*, *30*(2), 165–181.

Chance, K., and R. Kurucz (2010), An improved high-resolution solar reference spectrum for Earth's atmosphere measurements in the ultraviolet, visible, and near infrared, *J. Quant. Spectrosc. Radiat. Transfer*, *111*(9), 1289–1295.

Davis, C., et al. (2002), Ocean PHILLS hyperspectral imager, *Opt. Express*, *10*(4), 210–221.

Fontenla, J., J. Harder, W. Livingston, M. Snow, and T. Woods (2011), High-resolution solar spectral irradiance from extreme ultraviolet to far infrared, *J Geophys Res.*, *116*, D20108, doi:10.1029/2011JD016032.

Gao, B.-C., and C. O. Davis (1997), Development of a line-by-line-based atmosphere removal algorithm for airborne and spaceborne imaging spectrometers, *Proc. SPIE*, *3118*, 132–141.

Hamlin, L., R. Green, M. Eastwood, W. Hartford, and I. McCubbin (2010), Imaging spectrometer science measurements for terrestrial ecology: AVIRIS and next generation AVIRIS characteristics and developmental status, *NASA ESTF2010*, Jet Propul. Lab., Paseda, Calif.

Hochberg, E. J., et al. (2011), HyspIRI sun glint report, *JPL Publ. 11-4*, Jet Propul. Lab., Paseda, Calif.

Kohler, D., W. Bissett, R. Steward, and C. Davis (2004), New approach for the radiometric calibration of spectral imaging systems, *Opt. Express*, *12*(11), 2463–2477.

Kurucz, R. L. (2005), *Solar Spectrum Obtainable in MODTRAN 5.2.1*. [Available at http://kurucz.harvard.edu/sun.html.]

Lee, Z., K. L. Carder, R. F. Chen, and T. G. Peacock (2001), Properties of the water column and bottom derived from Airborne Visible Infrared Imaging Spectrometer (AVIRIS) data, *J. Geophys. Res.*, *106*(C6), 11,639–11,651.

Lucke, R. L., M. Corson, N. R. McGlothlin, S. D. Butcher, D. L. Wood, D. R. Korwan, R. R. Li, W. A. Snyder, C. O. Davis, and D. T. Chen (2011), Hyperspectral imager for the coastal ocean: Instrument description and first images, *Appl. Opt.*, *50*(11), 1501–1516, doi:10.1364/AO.50.001501.

Marchenko, S. V., and M. T. DeLand (2014), Solar spectral irradiance changes during cycle 24, *Astrophys. J.*, *789*(2), 117, doi:10.1088/0004-637x/789/2/117.

Mouroulis, P., et al. (2014), Portable Remote Imaging Spectrometer coastal ocean sensor, *Appl. Opt.*, *53*(7), 1363–1380.

Stuffler, T., et al. (2007), The ENMAP hyperspectral imager—An advanced optical payload for future applications in Earth observation programmes, *Acta Astronaut.*, *61*(1), 115–120.

Thompson, D. R., B. C. Gao, R. O. Green, D. A. Roberts, P. E. Dennison, and S. R. Lundeen (2015), Atmospheric correction for global mapping spectroscopy, *Remote Sens. Environ.*, doi:10.1016/j.rse.2015.02.010, in press.

Thuillier, G., M. Hersé, D. Labs, T. Foujols, W. Peetermans, D. Gillotay, P. C. Simon, and H. Mandel (2003), The solar spectral irradiance from 200 to 2400 nm as measured by the SOLSPEC spectrometer from the ATLAS and EURECA missions, *Sol. Phys.*, *214*(1), 1–22.

Wallace, L., K. Hinkle, W. Livingston, and S. Davis (2011), An optical and near-infrared (2958-9250 å) solar flux atlas, *Astrophys. J. Suppl. Ser.*, *195*(1), 6.

Warner, R. A., and C. Fan (2013), Optical spectra of phytoplankton cultures for remote sensing applications: Focus on harmful algal blooms, *Int. J. Environ. Sci. Dev.*, *4*, 94–98.